Real-Time Demultiplexer for Mixed-Frequency Acoustic Signals

Xinglu Ji(季星露), Haoxiang Li(李澔翔), Biao Wang(王标), Jiaming Zhang(张珈铭), Jie Hu(胡洁)*

College of information science and technology&College of artificial intelligence, Nanjing Forestry University, Nanjing, China

* Correspondence: hujie@njfu.edu.cn;

ABSTRACT: To achieve real-time frequency-division multiplexing for mixed-frequency acoustic signals and instantaneous information transmission, we present a demultiplexer based on a coiled labyrinth structure by means of spatial demultiplexing. The structure is composed of six coiled channels of varying lengths, embedded in the wall of the waveguide at a subwavelength scale. Leveraging localized resonance characteristics, the device separates and traps acoustic waves of different frequencies within specific channels. Unlike conventional rainbow trapping primarily aimed at energy dissipation, this design directly enables mixed-frequency acoustic signal demultiplexing, harnessing the intrinsic frequency-space mapping for information decoding. Numerical simulations demonstrate that the six distinct frequency components of the acoustic signal are guided into different curled channels, facilitating spectral demultiplexing. This physical separation is the basis for information transmission, a capability that extends to the efficient transfer of digital image data. Despite its low structural complexity and compact footprint, the device retains the capability to demultiplex multi-frequency acoustic signals and achieves high-performance signal transmission. Moreover, demultiplexing is performed instantaneously by the device without additional digital signal processing, embodying the “structure-as-function” design philosophy. This paradigm offers a novel approach to acoustic materials for information transmission and signal processing, heralding the prospect of their practical application in real-time acoustic communication.

PACS codes: 43.60.+d, 43.20.+g
Keywords: frequency-division multiplexing, signal demultiplexing, acoustic image transmission, coiled structures

1. Introduction

In the realm of acoustic information processing systems, acoustic demultiplexing technology serves as an indispensable bridge between the acoustic carrier and the extraction of effective information[1-3]. The performance of this technology directly influences the real-time capability, reliability, and the overall integration level of acoustic systems[4-7]. Consequently, it plays a vital role in fields such as advanced communications and sophisticated sensing technologies. Conventional approaches to acoustic signal demultiplexing have heavily relied on intricate electronic circuitry and digital signal processing algorithms which not only increases system complexity, but also inherently limits the practical deployment and real-time performance, particularly in applications demanding instantaneous response and miniaturization.

In recent years, acoustic metamaterials have gained significant attention as a promising avenue to overcome the limitations of natural materials[8-13]. Through sophisticated design strategies, these materials exhibit novel physical parameters not found in nature, thereby enabling precise manipulation of acoustic waves[14-16]. A key phenomenon exploited is the acoustic rainbow[17-20], which relies on depth-varying-index structures that leverage the differential propagation velocities of acoustic waves at different frequencies[21-25]. This effect allows for the spatial separation and trapping of sound waves, demonstrating substantial potential for diverse acoustic applications [26-29]. For instance, Zhou et al. achieve precise acoustic rainbow trapping in the low-frequency regime using micro Mie resonance structures for acoustic detection and filtering[30]. Similarly, Lu et al. realize acoustic rainbow trapping in three-dimensional space using a depth-varying groove design, showcasing promising prospects for applications in acoustic filtering and absorption[31].Building upon this principle, coiled configurations have emerged as a promising structural approach due to their unique advantages in achieving highly compact dimensions and efficient acoustic wave manipulation, making them particularly effective for realizing the acoustic rainbow effect[32-34]. Furthermore, the coiling space extends the acoustic propagation path, enabling a high acoustic refractive index at subwavelength scales[35-38], which significantly results in wave deceleration and localized resonance within a compact physical footprint[39-42]. For example, Ni et al. demonstrate rainbow trapping of low-frequency broadband acoustic waves using coiled structures, thereby advancing the application of this technology in compact devices[43]. The coiled meta-silencer proposed by Krylov et al. and Mousavi et al. , which combine rainbow trapping with the acoustic black hole effect, achieved broadband low-frequency noise control, further validating the efficacy of coiled structures for acoustic manipulation[44, 45].

In the context of acoustic rainbow trapping, a phenomenon where acoustic waves of different frequencies are spatially separated and trapped within depth-varying-index structures, a crucial aspect has often been overlooked: the inherent one-to-one correspondence between frequency and spatial location. This precise frequency-space mapping constitutes the foundational basis for acoustic demultiplexing. However, a gap remains between this inherent mapping relationship and the functional demands of information demultiplexing in current studies. As a result, the broader application

potential of acoustic rainbow trapping for real-time decoding of multi-frequency acoustic signals, a paradigm shift from conventional electronic or digital processing methods, has not yet been fully realized. To address these challenges, we present a passive acoustic demultiplexer based on a coiled labyrinth structure. Unlike conventional digital signal processing based approaches, which involve analog-to-digital conversion, data buffering, and fast-Fourier-transform based processing with latencies on the order of milliseconds and power consumption of tens to hundreds of milliwatts, our device accomplishes the demultiplexing task directly at the physical layer. The signal latency is governed solely by the acoustic propagation time through the coiled channels, ranging from 39 μs to 97 μs, which is lower than that of typical DSP implementations. Meanwhile, the passive structure eliminates standby power consumption and reduces hardware complexity, offering a distinct advantage for compact and energy-efficient acoustic communication systems. Through precise tuning of the path lengths in each coiled channel, localized resonance characteristics are engineered such that acoustic waves of different frequencies are intrinsically separated and directed to predetermined outlets. This fully passive process avoids the need for electronic components and complex algorithms, enabling instantaneous demultiplexing at subwavelength scales without additional digital signal processing.

2. Theory and model

The schematic of the proposed two-dimensional acoustic metamaterial-based demultiplexing device is illustrated in Fig. 1. The device comprises six space-coiling units attached to the wall of the waveguide with a width of w_1. The length of the coiling units on both sides of the waveguide increases progressively from L_1 to L_6, with a center-to-center spacing distant between adjacent units of a and the thickness of the wall between them is t_1. Within each coiled unit, the horizontal plates have a thickness of t_2, and the air channels have a width of w_2. Acoustic waves propagate along a zigzag path within these channels, resulting in an effective propagation path length, denoted as L_i, for each unit.

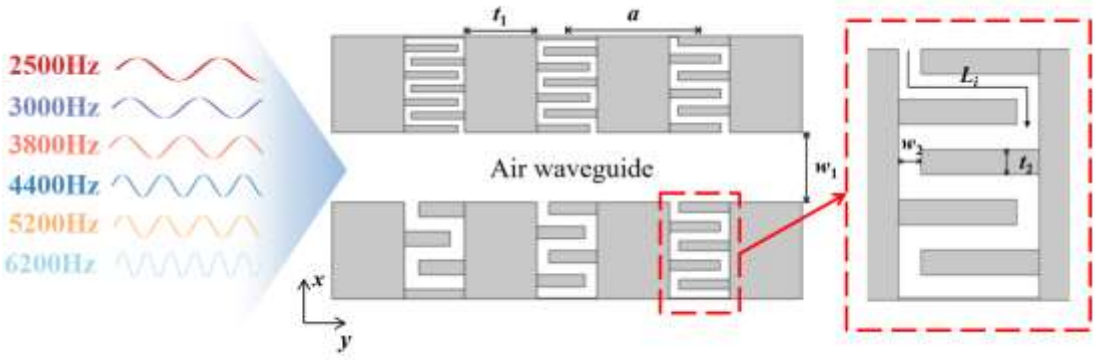


Fig.1 Schematic Diagram of the Real-Time Acoustic Demultiplexing Structure.

The channel path length L_i is designed to satisfy the half-wavelength resonance condition for a specific acoustic wavelength. Owing to its reflective termination, each coiled channel can be equivalently modeled as a quarter-wavelength resonator. When

the incident acoustic wave frequency matches the resonant frequency of a specific channel, a pressure antinode is formed at the closed end and a node is formed at the open entrance. This standing wave pattern results in the strong localization of acoustic energy, thereby achieving the trapping of specific frequency components. The depth-varying design yields air channel lengths L_1 to L_6 of 13.83 mm, 16.49 mm, 19.49 mm, 22.57 mm, 28.58 mm, and 33.24 mm, respectively. The corresponding resonant frequencies for the six channels are 6200 Hz, 5200 Hz, 4400 Hz, 3800 Hz,3000 Hz, and 2500 Hz, which enables the spatial separation of multi-frequency acoustic waves. The overall structural length is approximately half of the acoustic wavelength at the highest operating frequency (6200Hz), ensuring the device's subwavelength characteristics.

As shown in Fig. 2(a), the acoustic dispersion curves for channel units of varying lengths are calculated using the finite element method. The black dash line corresponds to the dispersion curve of air, while the remaining curves represent the dispersion relations for the different channel units, which reveals that all dispersion curves exhibit a similar trend. In the small-wave-vector regime, the curves nearly coincide with the air dispersion line. As the wave vector increases, they gradually deviate from the reference in air and become increasingly flat. As the wave vector approaches the Brillouin zone boundary, the dispersion curves asymptotically approach a horizontal slope.

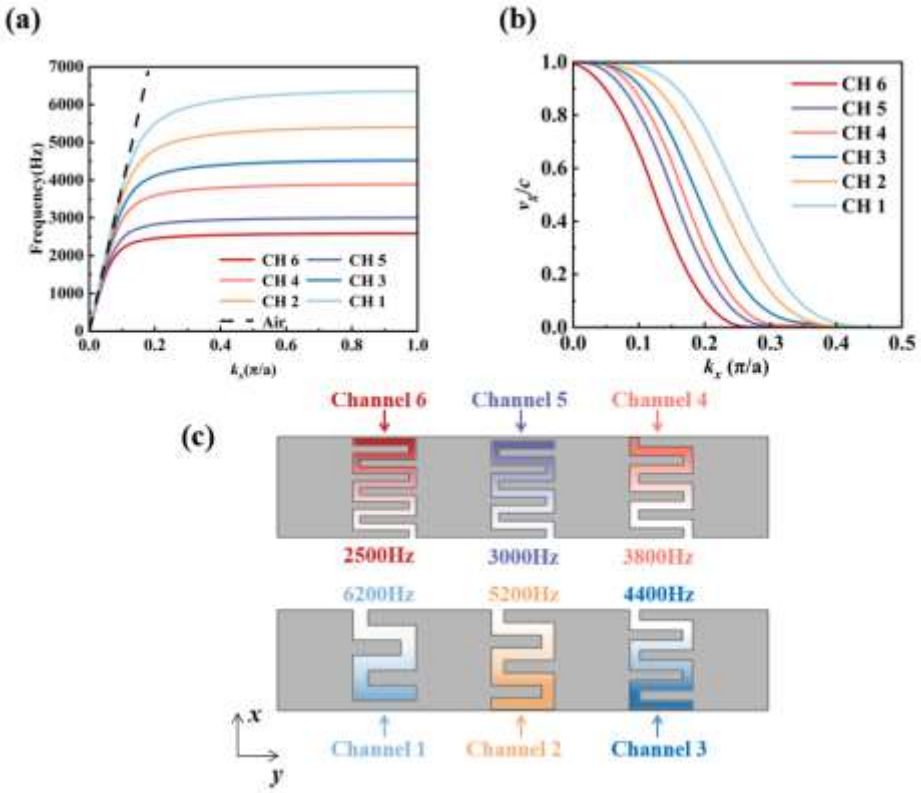


Fig.2 (a) Dispersion relations of the coiled structure with different channel depths (b) Calculated group velocities (normalized to the speed in air) as a function of the wave vector k_x for the six coiled channels with different lengths of CH 1 to CH 6. (c)Simulated amplitude distribution along the depth-varying groove surface.

According to the expression for the group velocity of acoustic wave propagation:

$$v_g = \partial\omega / \partial k_x \quad (1)$$

, in which $\omega = 2\pi f$ is the angular frequency, f is the operating frequency, and k_x is the wave number in the medium, a horizontal dispersion curve indicates a near-zero group velocity in Fig.2(b). The frequency at which this flattening occurs is identified as the cutoff frequency for the respective channel. The group delay associated with each coiled channel can be estimated as

$$\tau_g = L_i / v_g \quad (2)$$

in which L_i is the effective acoustic length of the channel. This quantity characterizes the time required for an acoustic pulse to propagate through the channel and is used to quantify the real-time response of the demultiplexer. The calculated values range from 39 μs (CH1, 6352 Hz) to 97 μs (CH6, 2586 Hz). These delays confirm the real-time nature of the demultiplexing process.

Channel	Theoretical (Hz)	Simulated (Hz)
CH6	2586.3	2580
CH5	3000.7	3000
CH4	3888.8	3800
CH3	4520.4	4400
CH2	5299.2	5200
CH1	6352.2	6200

Table 1. Theoretically predicted and simulated resonance frequencies of the six channels.

To assess the validity of the Bloch dispersion analysis for the finite-sized device, we compare the resonance frequencies extracted from the full finite-structure simulations with those predicted by the infinite periodic unit-cell model. The results are summarized in Table 1, where the theoretical and simulated frequencies agree within 2% for all six channels, confirming the applicability of the infinite periodic dispersion analysis to the present finite-sized device, validating that each coiled channel effectively resonates at its designated frequency.

As confirmed by the simulated acoustic energy distributions in Fig. 2(c), incident waves at the six target frequencies are progressively slowed and trapped at distinct positions along the waveguide, with higher frequencies localized at shallower channel depths. This one-to-one frequency-to-position mapping directly manifests the strong dispersive behavior predicted by the group velocity analysis in Fig. 2(b).

3. Results and discussion

3.1. numerical demonstration

Following the theoretical analysis, finite element simulations are conducted to analyze the acoustic field distribution, thereby validating the capability of the proposed demultiplexer. The simulation model, based on the design in Fig. 1, is constructed with

the following parameters: The upper and lower channel arrays are designed for six target frequencies, with the key structural parameters specified as follows:w_1= 20 mm, w_2= 1.2 mm, t_1= 6 mm, t_2= 1.2 mm, and a = 10 mm, The material properties are defined as follows: the background air with a density ρ_{air} = 1.21 kg/m³ and its sound speed c_{air} = 343 m/s ; the material steel with a density ρ_{steel} =7800 kg/m³ and its sound speed is c_{steel} = 1635 m/s.

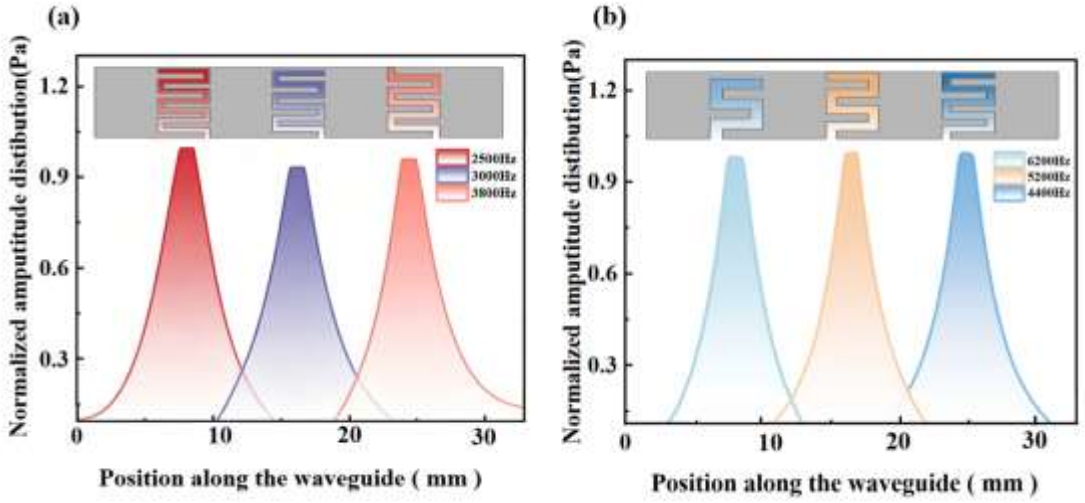


Fig. 3 (a) Simulated normalized amplitude distribution of incident acoustic waves along the upper depth-varying coiled channels. (b) Simulated normalized amplitude distribution of incident acoustic waves along the lower depth-varying coiled channels.

The acoustic amplitude distributions for six distinct frequencies within the structure are presented in Fig.3. The simulations reveal that each frequency component is progressively confined to a channel of a specific depth during propagation. Acoustic energy localization is observed to be maximal at the resonant frequency of each channel, signifying the effective spatial separation of the multi-frequency acoustic waves. This observed phenomenon is in excellent agreement with the theoretical predictions derived from the dispersion relationship, thereby validating the effectiveness of the depth-varying coiled structure for frequency-selective trapping.

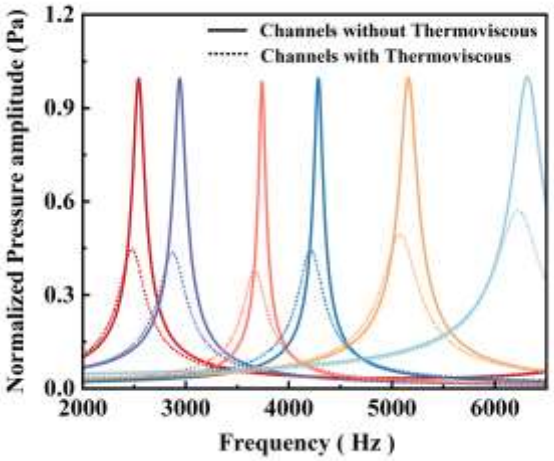


Fig.4 Frequency responses of the six channels with the lossless model (solid lines) and the thermoviscous model (dashed lines). Colors distinguish individual channels, ordered as CH6 to CH1 from left to right.

Meanwhile, to assess the influence of thermoviscous losses on the device performance, we further perform comparative simulations using the thermoviscous acoustic model. In the numerical model, the six coiled channels are modeled using the Narrow Region Acoustics feature with a slit height of 1.2 mm, which accurately accounts for the viscous and thermal boundary-layer dissipation effects arising from the narrow channel walls. The main waveguide is modeled using the standard pressure acoustics formulation, with plane-wave radiation boundary conditions imposed at both ends to emulate a free-field environment. The incident wave is applied normal to the left boundary of the waveguide and propagates rightward along the main channel. The entire computational domain is discretized with extremely fine unstructured meshes, with particular refinement applied inside the coiled channels and in the vicinity of the walls to ensure sufficient resolution of the thermoviscous boundary layers. As shown in Fig. 4, upon the inclusion of thermoviscous losses, the resonance frequencies of all channels exhibit deviations of less than 3% relative to the lossless model, while the peak amplitudes are moderately reduced. This frequency shift and amplitude attenuation arise from the viscous and thermal dissipation within the channels, which is physically expected in narrow-channel acoustic systems. Despite the moderate reduction in the maximum localized resonance amplitude, each channel maintains a clear frequency-selective response and spatial localization capability at its corresponding resonance frequency, confirming that the frequency-domain trapping and demultiplexing functionality remain well preserved under realistic loss conditions.

To evaluate the real-time information transmission of each channel and quantify the ring-up and ring-down times associated with the localized resonances, we perform time-domain simulations in which pulse trains are incident from the left boundary of the waveguide. The total simulation time is 150 ms, with a time step of 10 μs, ensuring adequate temporal resolution to resolve the carrier cycles and the envelope evolution. A 3-bit sequence is assigned to each frequency component, where code ‘1’ denotes the presence of the carrier signal and code ‘0’ indicates its absence. The encoded sequences for the six components (2500 Hz, 3000 Hz, 3800 Hz, 4400 Hz, 5200 Hz, and 6200 Hz) are 001, 010, 011, 100, 101, and 110, respectively. Each symbol duration is set to T = 30 ms, which serves as the unit symbol period for the subsequent image transmission encoding.

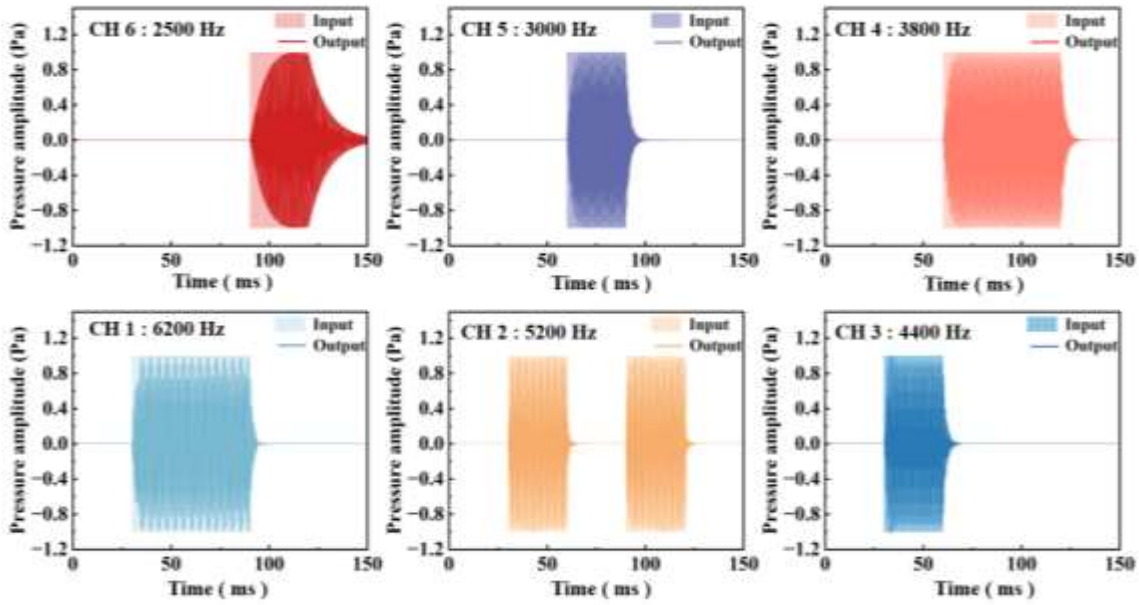


Fig.5 Time-domain signals received at the bottom of each of the six coiled channels in response to a multi-frequency input pulse.

The acoustic pressure responses are recorded at the closed ends of the corresponding coiled channels, from which the ring-up and ring-down times are extracted as the time required for the envelope to rise from 10% to 90% of the steady-state amplitude and to decay from 90% to 10%, respectively. As shown in Fig. 5, each channel exhibits a clear build-up of the resonance amplitude upon pulse arrival at the channel's resonant frequency, followed by a decay after the pulse ceases. The measured ring-up and ring-down times for the six channels are shorter than the 30 ms symbol duration by a significant margin, confirming that the symbol period is sufficiently longer than the cavity lifetime to ensure negligible inter-symbol interference. The output waveforms exhibit high temporal consistency with the frequency components of input pulses, which directly validates the structure's efficient capability for capturing and transmitting signals at its resonant frequencies.

Notably, the entire demultiplexing process is instantaneously completed at the physical level by the passive metamaterial structure itself, without requiring external digital signal processing or electronic components. Once the input pulse signal reaches the receiving end, each channel generates a nearly delay-free response that is synchronized with the input pulses. This demonstrates that the mechanism for mixed-signal separation and information extraction stems from the inherent physical interaction between the acoustic waves and the metamaterial structure. The operational principle of the entire system embodies a "structure-as-function" paradigm, wherein acoustic waves of specific frequencies are captured by their corresponding resonant channels, leading to energy localization. This process directly maps frequency information to spatial location and energy amplitude at the physical level, thereby enabling direct readout by individual sensors.

3.2. Image Information Transmission Based on Spatial Pixel Mapping

To validate the capability of the demultiplexer for multi-channel parallel information transmission, we use it to transmit and reconstruct simple character images using acoustic waves. The characters "N" and "J" are selected for transmission and encoded into 6×6 binary pixel matrices, where '1' represents an active (black) pixel and '0' represents an inactive (white) pixel. The specific encodings are as follows. The specific encodings are as follows: the character "N" corresponds to the six-row pixel sequences: "110011", "111011", "111111", "111111", "110111", "110011". The character "J" corresponds to: "111111", "111111", "000110", "100110", "111110", "011100".

The core functionality of this device is enabled by its six physical channels, which collectively function as a parallel acoustic data bus. As illustrated in Fig. 6(a), each acoustic channel simultaneously transmits two rows of pixel information from the character images. The pixel data for the characters "N" and "J" correspond to the three acoustic channels at the upper and lower ends of the structure, respectively. The entire image transmission is accomplished by transmitting six sets of consecutive time-domain pulse signals in six different channels.

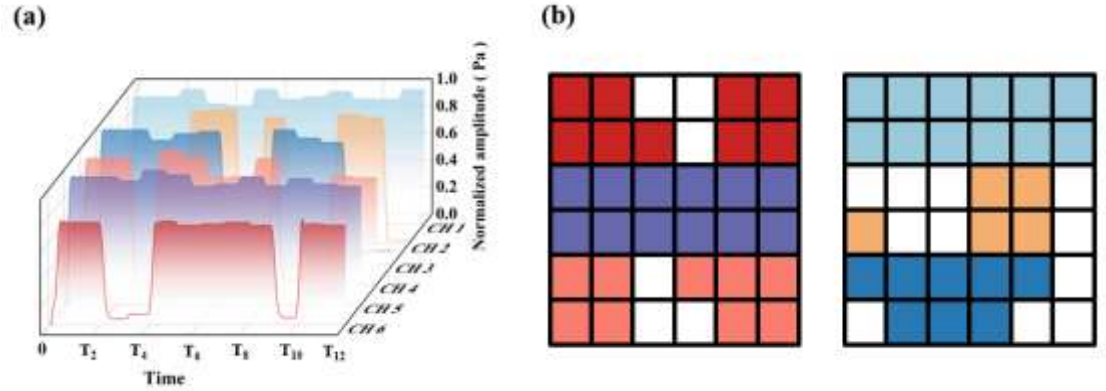


Fig.6 (a) Output responses at the bottom of the six channels; (b) Image obtained after demultiplexing.

The simulation results demonstrate that the output pulses from the six channels accurately replicate the input pixel-encoding sequences. For instance, Channel 6 outputs a high level ('1') at $t = T_1$, a high level ('1') at $t = T_2$, and subsequently outputs '0011111011' from $t = T_3$ to $t = T_{12}$. This output sequence is entirely consistent with the preset encoding "110011111011". The remaining channels exhibit comparable accuracy in reproducing their respective encoded sequences.

Although the peak amplitudes vary moderately across the six channels, the demodulation employed here does not require uniform absolute amplitudes. Instead, it relies on the contrast between the resonant and off-resonant states within each individual channel.

(a)

Channel	CR (dB)	SNR (dB)
CH 1	-15.24	25.73
CH 2	-16.29	26.42
CH 3	-17.68	26.55
CH 4	-17.25	26.61
CH5	-18.91	26.90
CH 6	-19.37	27.34

(b)

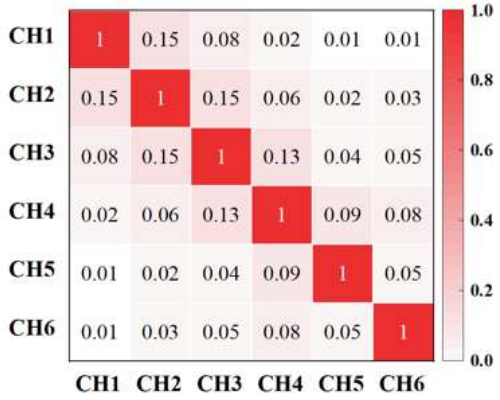


Fig.7 (a) Crosstalk Ratio and Signal-to-Noise Ratio of the six Channels. (b) Correlation coefficients between the signal responses of the six coiled channels. The color scale represents the correlation coefficient value, ranging from 0 (white, uncorrelated) to 1 (red, perfectly correlated).

To evaluate the performance of the demultiplexer in multi-channel communication systems, a quantitative analysis is conducted using two key metrics: channel isolation and noise immunity. Channel isolation is quantified using the Crosstalk Ratio (CR), which reflects signal leakage between adjacent channels. Noise immunity is characterized by the Signal-to-Noise Ratio (SNR), which measures the ability to accurately identify signals against background noise. The power values are recorded after the acoustic pressure transmission reach a steady state, and the crosstalk for each channel is calculated, as summarized in Fig.7(a).

To quantify the channel isolation, the crosstalk ratio (CR) is calculated using the following procedure. For each target CH_i, a continuous-wave excitation at its corresponding resonant frequency is applied at the waveguide inlet, while all other channel outlets are terminated as rigid walls. After the steady state is reached, the acoustic pressure amplitudes are recorded at the closed ends of all six channels. The CR for a specific channel is calculated using the formula $CR = 10\,log_{10}(P_{CH \neq CH\,i}/P_{CH = CH\,i})$, where $P_{CH \neq CH\,i}$ represents the sum of the received power in $CH\,i$ when all channels except $CH\,i$ are individually activated, and $P_{CH = CH\,i}$ denotes the received power in $CH\,i$ when only CH_i is activated.The SNR is defined as $SNR = 10\,log_{10}(P_{CH = CH\,i}/P_{noise})$ where P_{noise} is obtained by measuring the channel's baseline noise response under non-resonant frequency excitation.

Fig.7(a) indicates that the crosstalk for all six channels remains below -10 dB, while the SNR for each channel exceeds 25 dB, demonstrating excellent signal extraction capability in noisy environments. Fig.7(b) presents the correlation coefficients between the signal responses of the six coiled channels. In practical scenarios, the incident mixed-frequency signal interacts with all channels simultaneously, but one channel-engineered to match the resonant frequency of a specific component—exerts a dominant influence, enabling selective trapping and

separation. These metrics collectively validate the system's superior channel isolation and communication robustness. The aforementioned results demonstrate that the coiled-structure-based demultiplexer functions as an efficient acoustic information decoder. It spatially demultiplexes serially input mixed-frequency acoustic signals into multiple independent digital streams, which are output directly in parallel physical form. The entire demultiplexing process is entirely passive, requiring no analog-to-digital conversion or digital signal processing, thereby achieving end-to-end physical layer parsing from acoustic waves to digital information.

Next, we present a more practical demonstration by transmitting a complex binary image of 216×216 pixels, for which the emblem of Nanjing Forestry University is selected. As shown in Fig. 8(a), the image is divided into six sections and transmitted in parallel through six independent channels, with each channel carrying a 7774-bit 2ASK data stream. Fig. 8(b) presents an enlarged view of the specific square region marked by the yellow box in Fig. 8(a), where the binary digits "0" and "1" represent two distinct colors for each pixel. The decoded information for the four lines L1, L2, L3, and L4, extracted from the received time-domain signals, is presented in Fig. 8(c), alongside the target data streams for comparison. By assembling the data streams received at the bottom of the six channels, the reconstructed overall image is shown in Fig. 8(d).

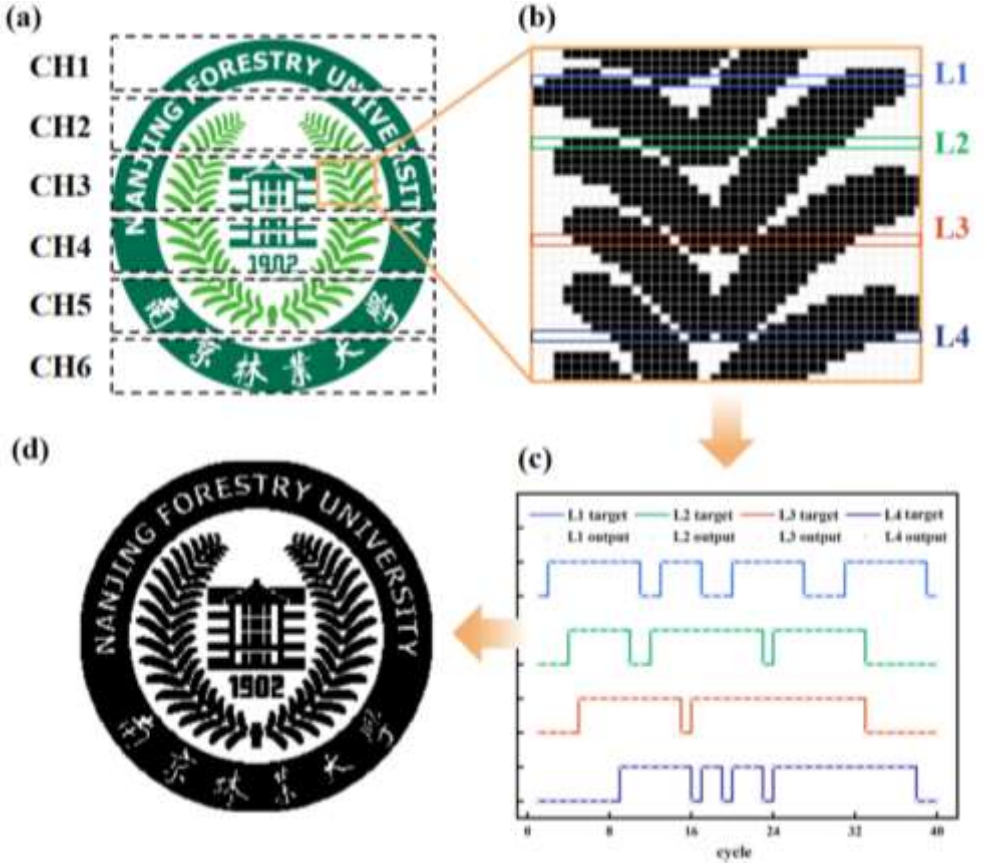


Fig.8 (a) The original input image which is divided into six separate parts for a parallel transmission along six independent channels (viz., CH1, CH2, CH3, CH4, CH5 and CH6 respectively). (b) The enlarged view of square region marked by yellow line in the two colors of pixel are encoded by binary information “0” and “1”. (c) The target

and output data streams of four lines in b, marked by L1, L2, L3, and L4. (d) The output image reconstructed from four data streams received in real-time by six sensors located at focal points. Permissions for use of the Nanjing Forestry University logo in this figure were obtained from Nanjing Forestry University. All rights reserved.

The results indicate that the primary image content is successfully recovered, providing preliminary evidence for the feasibility of this structure in transmitting image information with a certain degree of complexity.

4. Conclusion

In summary, a mixed-frequency acoustic demultiplexing device based on a coiled labyrinth structure has been designed, achieving real-time information demultiplexing and signal transmission. These functionalities are realized through localized resonance, whereby acoustic waves of different frequencies are trapped in channels corresponding to their respective cutoff frequencies. Numerical simulations demonstrate that the device effectively separates acoustic waves at six specific frequencies from 2.5 kHz to 6.2 kHz, with each component being strongly localized within its designated channel. Time-domain simulations further validate the structure's capability to demultiplex mixed-frequency signals. The successful transmission of the "NJ" characters and image signal demonstrate the excellent performance in signal transmission and this real-time demultiplexing is accomplished without external digital processing. This study provides new insights into the application of acoustic metamaterials in communications and signal processing. Furthermore, the operating frequency band can be tuned by adjusting the coiled channel paths in accordance with the half-wavelength resonance principle. Our results highlight the potential of the proposed demultiplexer as a foundational platform for passive, high-density acoustic information processing. This "structure-as-function" paradigm holds promise for diverse applications. Future work may focus on expanding its utility in areas such as compact acoustic data links, integrated sensing-communication nodes, and hardware-level preprocessing units for simplifying subsequent digital signal processing chains.

References

[1] Lu Y L, Zhu T, Chen L, and Bao X Y 2010 J. Lightwave Technol. 28 3243

[2] Wang L H V and Hu S 2012 Science 335 1458

[3] Ren X Y, Wang J, Liang Y J, Ma L H, and Zhou W 2024 Thin-Walled Structures 198 111683

[4] Bao X Y and Chen L 2012 Sensors 12 8601

[5] Fang G S, Xu T W, Feng S W, and Li F 2015 J. Lightwave Technol. 33 2811

[6] Shi C Z, Dubois M, Wang Y, and Zhang X 2017 Proc. Natl. Acad. Sci. U.S.A. 114 7250

[7] Jiang X, Liang B, Cheng J C, and Qiu C W 2018 Adv.Mater. 30 1800257

[8] Lai Y, Wu Y, Sheng P, and Zhang Z Q 2011 Nat.Mater. 10 620

[9] Zhang S, Xia C G, and Fang N 2011 Phys. Rev. Lett. 106 024301

[10] Christensen J and de Abajo F J G 2012 Phys. Rev. Lett. 108 124301

[11] Mei J, Ma G C, Yang M, Yang Z Y, Wen W J, and Sheng P 2012 Nat.Commun. 3 756

[12] Huang Y H, Lv M Y, Luo W J, Zhang H L, Geng D X, and Li Q 2021 J.Phys.D:Appl.Phys. 55 045104

[13] Yang Y, Tu J, Shan M L, Zhang Z J, Chen C, and Li H X 2025 Ultrason.Sonochem. 114 107261
[14] Popa B I and Cummer S A 2014 Nat.Commun. 5 3398
[15] Tian Z H, Shen C, Li J F, Reit E, Gu Y Y, Fu H, Cummer S A, and Huang T J 2019 Adv.Funct.Mater 29 1808489
[16] Keogh M R and Bilal O R 2025 Proc. Natl. Acad. Sci. U.S.A. 122 e2502036122
[17] Tsakmakidis K L, Boardman A D, and Hess O 2007 Nature 450 397
[18] Gan Q Q, Fu Z, Ding Y J, and Bartoli F J 2008 Phys. Rev. Lett. 101 256803
[19] Gan Q Q, Ding Y J, and Bartoli F J 2009 Phys. Rev. Lett. 102 199
[20] Zhu J, Chen Y Y, Zhu X F, Garcia-Vidal F J, Yin X B, Zhang W L, and Zhang X 2013 Sci. Rep. 3 1728
[21] Robertson W M, Baker C, and Bennett C B 2004 Am. J. Phys. 72 255
[22] Krauss T F 2008 Nat. Photonics 2 448
[23] Santillán A and Bozhevolnyi S I 2011 Phys. Rev. B 84 064304
[24] Jia H, Lu M H, Ni X, Bao M, and Li X D 2014 J. Appl. Phys. 116 124504
[25] Elshahat S, Wang C Y, Zhang H Y, and Lu C C 2021 Appl. Phys. Lett. 119 230505
[26] Ma F Y, Wu J H, Huang M, Fu G, and Bai C G 2014 Appl. Phys. Lett. 105 213702
[27] Jiménez N, Romero-García V, Pagneux V, and Groby J P 2017 Sci. Rep. 7 13595
[28] Farid S, Dixon K, Shayegannia M, Ko R H H, Safari M, Loh J Y Y, and Kherani N P 2021 Adv. Opt. Mater. 9 2100695
[29] Soliman S E, Barlou M, Wong Z J, and Tsakmakidis K L 2025 Nat. Rev. Phys. 7 409
[30] Zhou C, Yuan B G, Cheng Y, and Liu X J 2016 Appl. Phys. Lett. 108 063501
[31] Lu Y X, Dong D X, Li X, Hu C J, Wang M Z, Chen C D, Liu Y W, Ji H L, and Fu Y Y 2025 Appl. Acoust. 231 110502
[32] Liang Z X, Feng T H, Lok S, Liu F, Ng K B, Chan C H, Wang J J, Han S, Lee S, and Li J S 2013 Sci. Rep. 3 1614
[33] Xie Y B, Popa B I, Zigoneanu L, and Cummer S A 2013 Phys. Rev. Lett. 110 175501
[34] Lee S, Jang J, and Song K 2025 Mech. Syst. Signal Process. 222 111744
[35] Li Y, Liang B, Zou X Y, and Cheng J C 2013 Appl. Phys. Lett. 103 63509
[36] Ma G C, Xiao M, and Chan C T 2019 Nat. Rev. Phys. 1 281
[37] Xu J-H, Zhu X-F, Chen D-C, Wei Q, and Wu D-J 2022 Chinese Physics B 31
[38] Wang X, Dong R Z, Li Y, and Jing Y 2023 Rep. Prog. Phys. 86
[39] Liu Z Y, Zhang X X, Mao Y W, Zhu Y Y, Yang Z, Chan C T, and Sheng P 2000 Science 289 1734
[40] Ma G C and Sheng P 2016 Sci. Adv. 2 e1501595
[41] Jang J Y, Park C S, and Song K 2022 Mech. Syst. Signal Process. 178 109270
[42] Liu X W, Liu M L, and Xin F X 2023 Mech. Syst. Signal Process. 185 109762
[43] Ni X, Wu Y, Chen Z G, Zheng L Y, Xu Y L, Nayar P, Liu X P, Lu M H, and Chen Y F 2014 Sci. Rep. 4 7038
[44] Krylov V V and Tilman F J B S 2004 J. Sound Vib. 274 605
[45] Mousavi A, Berggren M, and Wadbro E 2022 J. Acous. Soc. Am. 151 4279

Acknowledgements

This work is supported by the National Natural Science Foundation of China (grant no.

12374416,12504518), the Natural Science Foundation of Jiangsu Province (grant no. BK20240659, BK20233001).

Data Availability

All the data during this study are available in the paper. Additional data related to this paper are available from the corresponding authors upon reasonable request.